ADVANCED MATERIALS INTERFACES
www.advmatinterfaces.de



# Exploring Electron Transport and Memristive Switching in Nanoscale Au/$WO_x$/W Multijunctions Based on Anodically Oxidized Al/W Metal Layers

*Maria Bendova, Jaromir Hubalek, and Alexander Mozalev**

**An array of semiconducting tungsten-oxide ($WO_x$) nanorods, 100 nm wide and 700 nm long, is synthesized via the porous-anodic-alumina-assisted anodization of tungsten on a substrate and is modified by annealing in air and vacuum. The rods buried in the alumina nanopores are self-anchored to the tungsten layer while their tops are interconnected via gold electrodeposited inside and over the pores. Thus formed metal/semiconductor/metal microdevices are used for studying electron transport within the nanorods and across the multiplied nanoscale Au/$WO_x$ and W/$WO_x$ interfaces. The dominating effect of a Schottky junction that forms at the Au/$WO_x$ interface is justified for the as-anodized and air-annealed nanorods tested at room temperature, which transforms into an ohmic contact at elevated temperature, whereas the bottom W/$WO_x$ interface turns out to be Schottky-like and govern the electron transport, giving a higher barrier and a set of pronounced diode-like characteristics in the as-anodized nanoarrays. The amorphous nanorods reveal bipolar resistive switching with a gradual reset due to the field-driven movement of oxygen vacancies and induced modifications of the Au/$WO_x$ Schottky interface. The unique electrical and interfacial properties of the nanoscale Au/$WO_x$/W multijunctions form a basis for their application in emerging resistive random access memories or 3D gas-sensing nanodevices.**

## 1. Introduction

Nowadays, tungsten trioxide in its stoichiometric and sub-stoichiometric forms (hereafter $WO_x$) is gaining much attention due to useful inherent properties, including electrochromic, photocatalytic, sensing, and photoelectrochemical, making it suitable for diverse potential applications.[1] Nanostructuring of $WO_x$ in the size order of about 100 nm is expected to substantially enhance or modify its surface properties due to the increased surface-to-volume ratio, altered surface energies, and the weak quantum size effect.[1–3] Eventual functionalization of $WO_x$ nanostructures through modifying the surface and interfacial properties by combining, doping, or decorating the pure oxide with other nanomaterials creates additional metal/semiconductor or semiconductor/semiconductor interfaces and grain boundaries capable of further influencing the sensing, electrical, optical, and opto-electronic properties or even introducing novel unique functionalities.[4–6]

Contrarily to $WO_x$ nanostructures with no directional orientation of its morphological units, like disordered 1D nanowires or nanorods grown by vapor- and liquid-phase methods,[1,7] oriented 1D $WO_x$ nanostructures, self-organized and upright-standing on a conducting substrate, without mutually intersecting with each other are expected to bring more advantages for practical applications in nanoscale electrochromic,[8,9] field-emission,[10] gas-sensing,[11] and photonic devices. Moreover, substrate-supported 1D nanostructures assembled in an array would enable the use of their integral properties, especially electrical, optical, or mechanical in contrast with the formation and application of single nanowires relying on their individual characteristics.[12,13] Synthesis of $WO_x$ nanostructures regularly aligned on substrates has been an active and competitive area of nanoscience and nanotechnology as the arrays of 1D structures often suffer from mechanical weakness and randomly dispersed physical contacts between neighboring units, limiting their performance in a device. Besides, creating well-defined nanoscale metal/semiconductor electrical and thermal interfaces and boundaries by contacting the tops of 1D nanostructures assembled in an array in a reliable and reproducible manner to benefit from the characteristics measured along the nanostructures and across relevant interfaces has been a challenge.[8–11,14–17]

Surface engineering of aluminum[18] and porous anodic alumina (PAA) films grown by anodic oxidation (anodizing) of aluminum have been of increasing interest for lithography-free templating of metals, dielectrics, and semiconductors.[19–22] PAA-assisted anodization[23] of certain valve metals sputtered on substrates, including tungsten,[24–26] has proven its potential as a reproducible method for electrochemically forming self-organized vertically aligned spatially separated 1D nanostructures (nanocolumns, rods, or tubes), being nearly ideally electrically and mechanically bonded at their bottoms either to the substrate metal[26] or to a continuous solid layer of similar metal oxide that grows at the columns/substrate-metal interface.[24,25] On the way

Dr. M. Bendova, Dr. J. Hubalek, Dr. A. Mozalev
CEITEC – Central European Institute of Technology
Brno University of Technology
Purkynova 123, Brno 61200, Czech Republic
E-mail: alexander.mozalev@ceitec.vutbr.cz



**DOI: 10.1002/admi.201600512**

of utilizing the PAA-assisted metal-oxide nanostructures and relevant electrical interfaces in emerging microdevices, we have recently incorporated arrays of PAA-assisted niobium-oxide nanocolumns[27] into a 3D architecture, in which a microstructured top Au electrode was formed onto the column tops, effectively making use of the whole length of all nanocolumns and involving nearly 100% of the upper metal/oxide interfaces in gas sensing.[28]

In the present work, we synthesized an array of $WO_x$ nanorods via a PAA-assisted anodization of thin tungsten layer in which, in contrast with the earlier works[24,25] the rods are well separated at their bottoms by the substrate metal and are not released from the PAA overlayer. In order to make contacts to tops of the nanorods and create patterned arrays of electrically active metal/semiconductor interfaces, we employed, for the first time, point electrodeposition of gold through a photoresist mask into the alumina nanopores onto the $WO_x$ nanorods and also over the alumina surface. To explore electrical transport properties and interfacial phenomena in thus formed metal/semiconductor/metal (MSM) microdevices, we carried out a deep investigation of electron transport along the $WO_x$ nanorods in an array and across the functional Au/$WO_x$ (upper) and W/$WO_x$ (bottom) interfaces at room and elevated temperatures, additionally modifying the film morphology, crystal structure, and chemical composition by annealing in air and vacuum. This allowed us to identify the transport-limiting Schottky junctions and their contribution to the integral transport processes at various operating temperatures and correlate the parameters of a depletion layer that forms at the Au/$WO_x$ interface with the crystal structures of differently prepared and annealed $WO_x$ semiconductor nanorods incorporated in the PAA matrix. The findings of this work helped experimentally justify the previously developed models of cooperative ionic transport through the respective interfaces during the film growth[24,26] and formulate the ideas for use of this advanced material in nanoscale electronic, sensing, and photoelectrochemical emerging devices.

## 2. Results and Discussion

### 2.1. Film Morphology, Structure, and Composition

Arrays of metal-substrate-supported $WO_x$ nanorods incorporated in a layer of nanoporous alumina were synthesized via so-called PAA-assisted anodization of a layer of tungsten sputtered on a substrate generally following the approach developed in our previous work[26] and adjusted here to meet the objectives of the present study (**Figure 1**). An Al/W bilayer sputtered on a dielectric substrate is first anodized to grow a PAA layer with well-ordered nanopores from the whole aluminum thickness (Figure 1b), this being followed by growth of $WO_x$ nanoprotrusions into the pores (Figure 1c). Further re-anodizing at certain conditions results in the growth of $WO_x$ at both the $WO_x$/W and electrolyte/$WO_x$ interfaces, as shown in Figure 1d, thus giving an array of pore-directed $WO_x$ nanorods anchored to the substrate metal (electron conductor) and deeply incorporated in the PAA layer (hereafter "PAA-inbuilt" nanorods). The situation when the tungsten-oxide nanorods grow directly from the tungsten metal without being merged in a metal-oxide layer at their bottoms has resulted from the set of technological, electrical, and electrolytic conditions developed in the previous work.[26] Scanning electron microscopy (SEM) images showing 3D views of the edges of samples having the PAA-inbuilt and PAA-free (alumina dissolved away) nanoarrays are displayed in **Figure 2**a,b, respectively. SEM images of cross fractures of the PAA-inbuilt nanoarrays accompanied by schematic drawings noticing the differences at the $WO_x$/W interfaces caused by the annealing conditions are shown in Figure 2c,e while the surfaces of the same PAA-free samples are shown in Figure 2d,f. In the images of PAA-inbuilt nanoarrays, some of the columns look disrupted across the film fracture, which is an artefact of the breaking. The smooth outer surface of the PAA-free nanorods is justified in Figure 2b.

As the first step in studying functional properties of the PAA-inbuilt $WO_x$ nanoarrays, the as-anodized, air-, and vacuum-annealed samples were characterized by means of electrical measurements in a solid-state MSM assembly. To this end, a layer of gold contacting the tops of the rods was formed via an original point electrodeposition technique, as depicted in Figure 1e, and served as an upper electrode while the tungsten underlayer was used as the bottom electrode.

From the previous SEM and X-ray diffraction (XRD) results,[26] the as-anodized amorphous oxide nanorods crystallize to $WO_{2.9}$ and a mixture of $WO_3$ and $WO_{2.9}$ phases due to the 550 °C annealing in vacuum and in air, respectively. During the heating in vacuum, the oxygen anions composing the rods are partly released into the gas phase[29] leaving an increased concentration of oxygen vacancies in the rods, this being accompanied by the formation of $WO_{2.9}$ phase. In case of the air-annealed nanorods, although the two phases are distributed along the whole length of the rods,[26] the $WO_3$ phase is likely to dominate at their tops while a higher concentration of $WO_{2.9}$ is expected in the vicinity of the bottom $WO_x$/W interface. The quantitative XRD analysis has shown that the $WO_3$

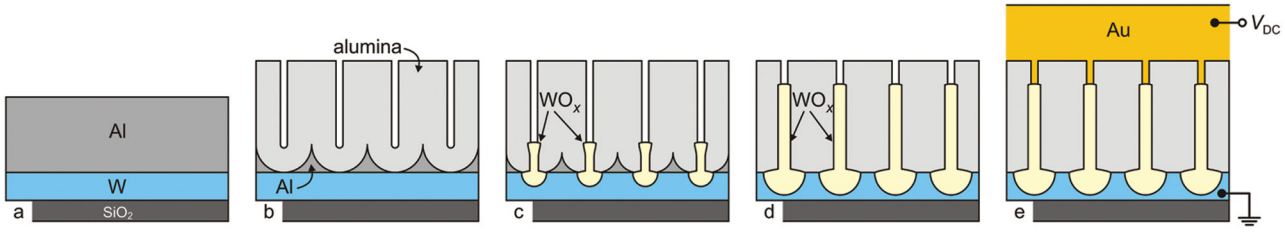


**Figure 1.** Process steps in fabricating a metal/semiconductor/metal (MSM) microdevice incorporating porous-anodic-alumina (PAA)-inbuilt $WO_x$ nanorods: a) sputter-deposition of an Al/W bilayer onto a $SiO_2$/Si wafer, b) porous anodization of the Al layer, c) anodization of the W layer through the PAA nanopores, d) re-anodization of the W layer for forming PAA-inbuilt $WO_x$ nanorods, followed by annealing in air or vacuum, and e) point electrodeposition of gold for forming top electrical contacts.

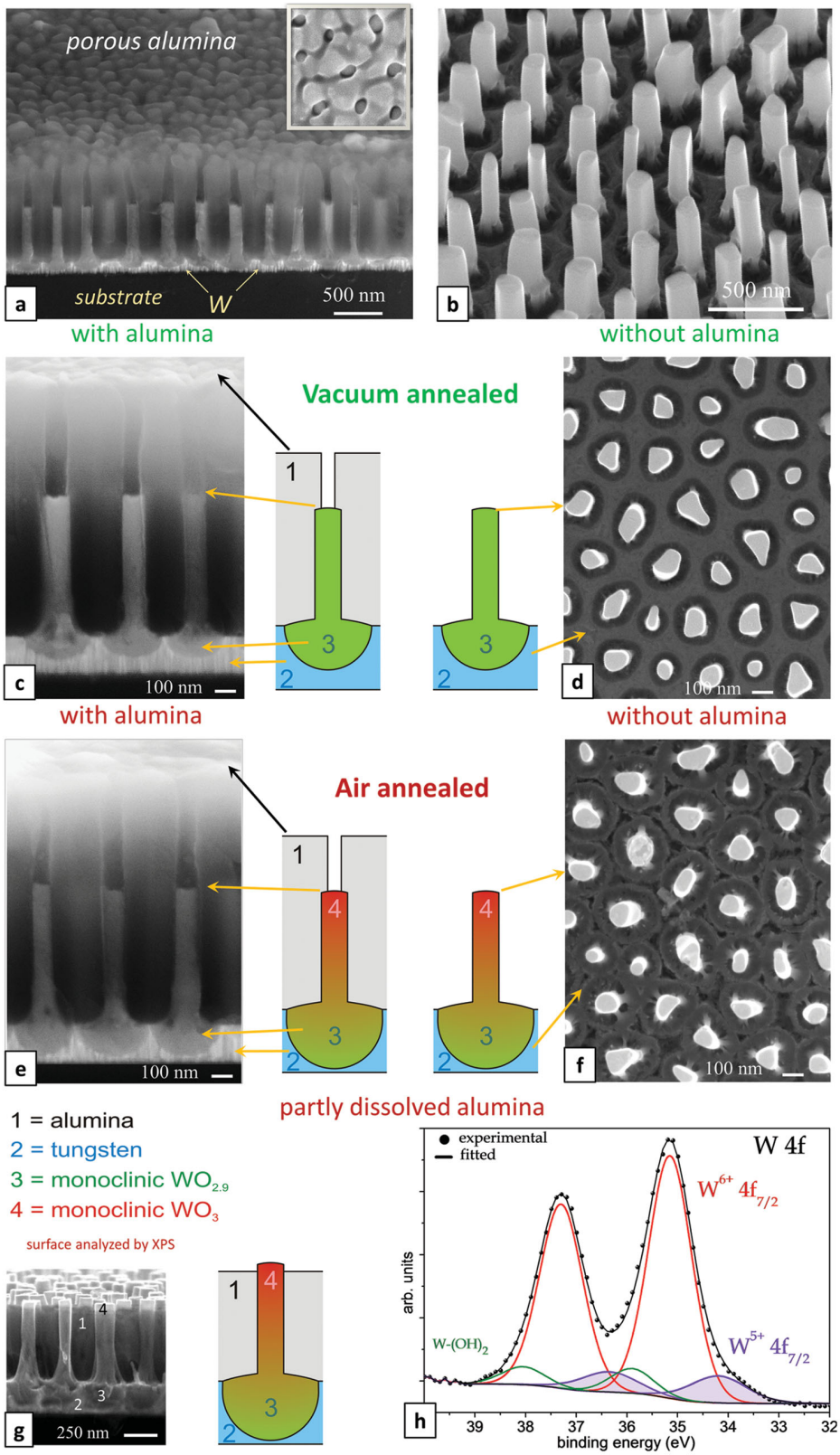


**Figure 2.** SEM 3D views of an edge of the sample having a) PAA-inbuilt and b) PAA-free (alumina dissolved away) $WO_x$ nanoarray; SEM images of c,e,g) cross-fractures and d,f) surfaces complemented by schematic representations of the PAA-inbuilt and PAA-free $WO_x$ nanorods annealed in vacuum ($10^{-4}$ Pa) and air at 550 °C showing relevant changes in film morphology and crystal structure; h) experimental and fitted W 4f XP core-level spectra of the air-annealed PAA-partly etched nanorods as SEM-viewed and depicted in panel (g).

  

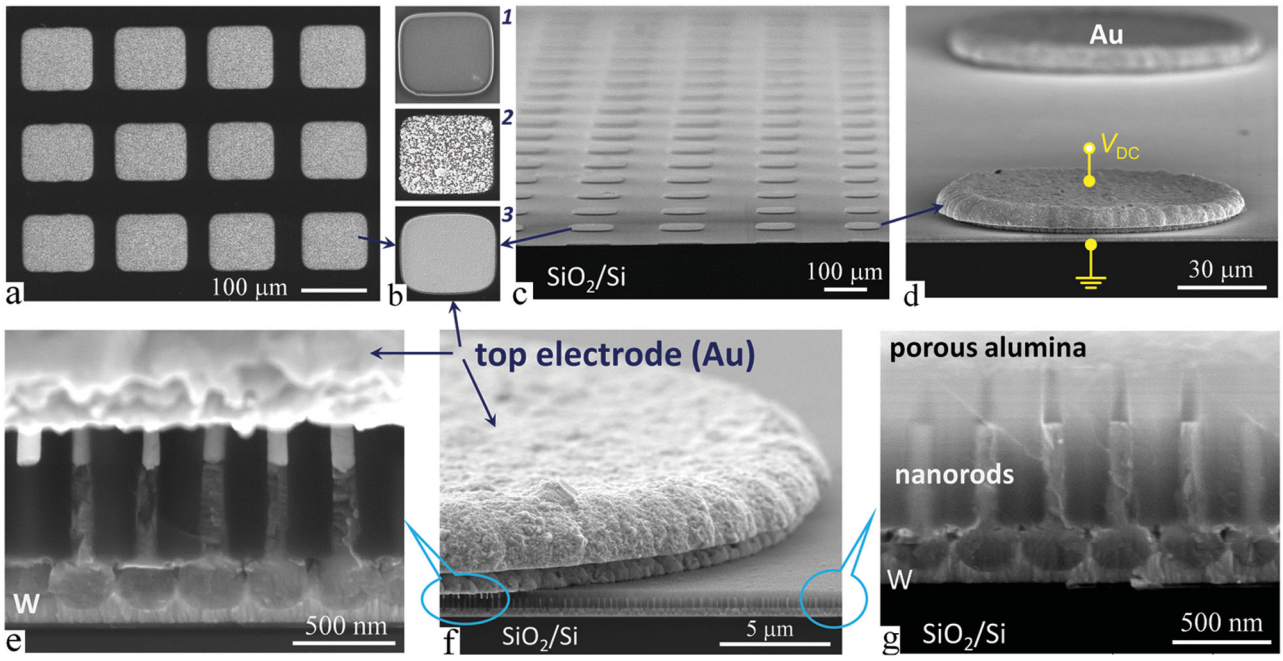


**Figure 3.** SEM views showing various process stages in micromachining PAA-inbuilt MSM devices: a,c,d) panoramic views of multiplied top Au electrodes of MSM microdevices, b) surface views of a window in the photoresist mask showing the development of a top Au electrode over the PAA surface: *1*) beginning of Au electrodeposition, *2*) incomplete Au deposition, *3*) complete Au deposition; e–g) fragments of cross fractures of a PAA-inbuilt nanorod array with and without a top Au electrode.

phase takes up about 70% of the rods' volume above the original W/Al interface.[26] This can be attributed to the annealing in oxygen-rich atmosphere leading to diffusion of oxygen into the rods, establishing an equilibrium concentration of oxygen vacancies,[29] and contributing to the expansion of bottom parts of the rods (Figure 2e). Concurrently, the diffusion of oxygen ions from the bottoms of rods into the metal substrate creates a higher concentration of oxygen vacancies there, which finally results in transformation into $WO_{2.9}$ phase near the oxide/metal interface.

Chemical composition of tops of the air-annealed nanorods was further confirmed by X-ray photoelectron spectroscopy (XPS) analysis performed for the sample with partly dissolved PAA layer, as SEM imaged and depicted in Figure 2g. The presence of carbon, tungsten, oxygen, aluminum, phosphorus, and silicon species was identified in the survey surface spectrum. All binding energies were referenced to the C 1s at 285.0 eV generated by photoelectrons emitted from carbon atoms in C—H bonds. The peak-fitting of C 1s spectra was done as described in a previous work.[27] Since the dominating contribution to oxygen and aluminum signals was obviously from the PAA surface, we did not analyze the O 1s and Al 2p narrow-scan spectra. As the C 1s, P 1s, and Si 2p spectra showed no peak already after the first Ar-ion sputter-cleaning cycle, we conclude that the carbon, phosphorus, and silicon species are present only in the outermost layer of organic contamination and are not incorporated in the film material. Thus, we analyzed the W 4f core-level spectrum (Figure 2h) to gain insight into chemical bonds of tungsten composing the tops of the nanorods. Three doublet peaks (W $4f_{7/2}$ and W $4f_{5/2}$) are used to reproduce the spectrum in Figure 2h. The W $4f_{5/2}$ peak for each species is constrained to be at a fixed energy increment of 2.15 eV above the W $4f_{7/2}$ peak, and the W $4f_{7/2}$/W $4f_{5/2}$ peak intensity ratio is fixed to 4:3, with full width at half maximum of 1.0 for $W^{6+}$ and 1.3 for $W^{(6-n)+}$ species. The highest-intensity doublet at 35.15 eV (W $4f_{7/2}$) is associated with photoelectrons emitted from $W^{6+}$ ions (dominating amount). The lowest-energy doublet at 34.2 eV (W $4f_{7/2}$), shifted to only −0.95 eV from the main component, may be associated with photoelectrons emitted from $W^{5+}$ (6 at%). The highest-energy low-intensity doublet at 35.9 eV (W $4f_{7/2}$) can be assigned to hydroxyl groups bonded with tungsten, W—$(OH)_2$.[26] The presence of $W^{5+}$ ions in the monoclinic $WO_3$ phase at the tops of the rods is due to a certain concentration of oxygen vacancies, capable of altering electrical properties of the MSM microdevices, as will be discussed in Section 2.2.

For statistical electrical measurements of the PAA-inbuilt $WO_x$ nanoarrays, multiplied square-shaped gold electrodes of sizes ≈100 μm × 100 μm were electrodeposited through a patterned layer of photoresist, as shown in Figure 1e. **Figure 3** shows SEM images of an air-annealed sample at various stages of assembling the MSM microdevices. At the commencement of electrodeposition, the gold ions discharge on the tops of the rods,[30] and an array of gold nanocolumns grows within the alumina pores to reach the surface of the PAA film. When the gold nanocolumns come out from the pores, they widen and soon merge to a complete, pancake-like solid layer over the general level of the alumina surface (Figure 3). The gold layer spread over the alumina surface creates an array of nanoscale Au/$WO_x$ junctions as well as forms micropads in the MSM microcells.

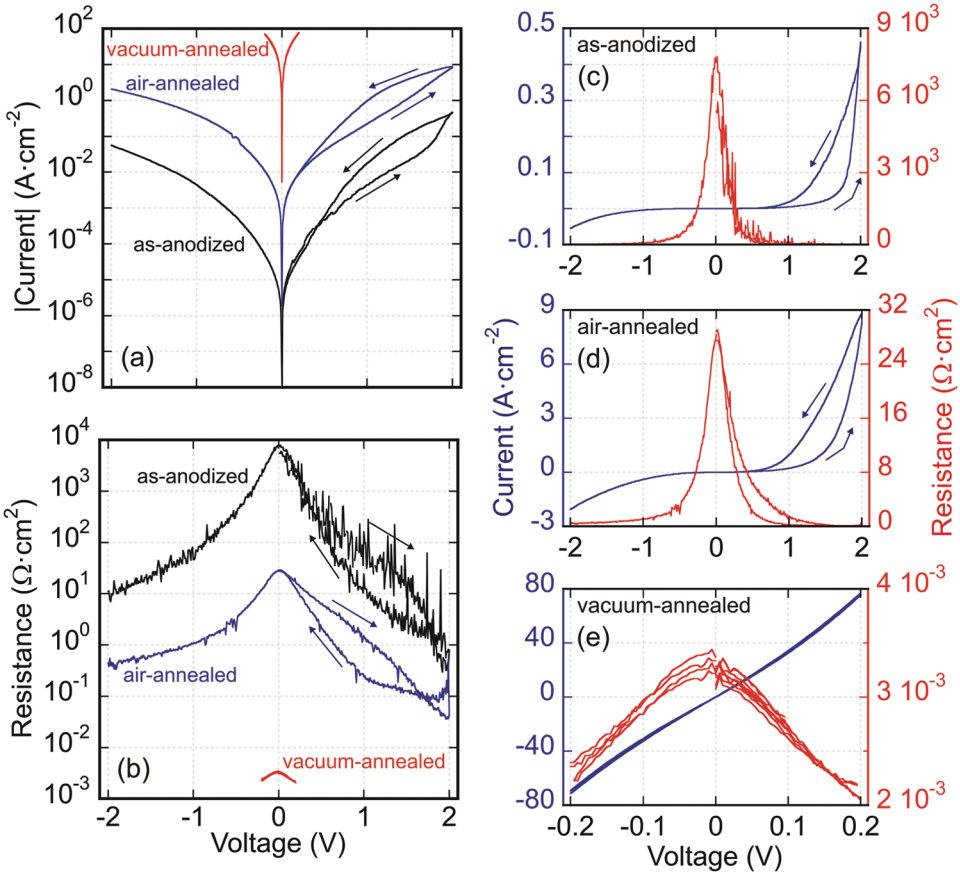


**Figure 4.** Experimental $I(V)$ and calculated $R_{dif}(V)$ curves recorded at room temperature (RT) for the as-anodized, air-annealed, and vacuum-annealed MSM microdevices, shown as a,b) semi-logarithmic and c–e) linear scale representations for each device type. The arrows point out the direction of voltage sweep under positive bias of the top Au electrode.

### 2.2. Electrical Properties

To determine basic parameters of the MSM microdevices and to model their behavior with an electrical circuit, current–voltage characteristics ($I(V)$ curves) were measured and presented as a dependence between the electric current passing through the device and the corresponding voltage applied across it. Three types of MSM microcells incorporating either the as-anodized, air- or vacuum-annealed $WO_x$ nanoarrays (shown in Figures 1e and 3) were measured by polarizing the top Au electrode while the tungsten underlayer was always grounded. **Figure 4**a compares typical $I(V)$ characteristics recorded at room temperature (RT) for the three types of MSM microcells, which are presented in logarithmic scale to better visualize the differences between the devices. As the $V$ and $I$ are not linearly proportional, the differential resistance, $R_{dif}$ ($dV/dI$), was calculated and plotted against the applied voltage as shown in Figure 4b. Additionally, the same data are presented as linear $I(V)$ and $R_{dif}(V)$ dependencies (Figure 4c–e) to emphasize the asymmetric behavior of the as-anodized and air-annealed devices. One may see that the current rises at a progressively increasing rate in the voltage range of 0 to ±2 V, being asymmetric at potentials over ±1.0 V and increasing more sharply at positive polarization of the top electrode. A hysteresis is also observed at the positive biases over 1.0 V, as indicated in Figure 4 by the arrows. In addition, the as-anodized and air-annealed samples when polarized at potentials over ±1.0 V show a systematic decrease in the resistance with consecutive measurement cycles. Therefore, only the initial measurements are shown in Figure 4. Notably, the resistance of the oxide nanoarrays decreases significantly from about $10^4$ to $10^{-3}$ Ω cm$^2$ in the following sequence: the as-anodized → air-annealed → vacuum-annealed samples.

The asymmetric $I(V)$ behaviors revealed for the as-anodized and air-annealed films are likely due to the formation of a rectifying Schottky junction at some of the $WO_x$/metal interfaces.[31,32] The directionality of thermionic current may provide an insight into the metal/semiconductor contact exhibiting the rectifying behavior.[32] In the present case of RT measurements, as the forward direction corresponds to the positive polarization of the top Au electrode, the Schottky-like barrier, being the limiting electron transport feature in the system, forms at the Au/$WO_x$ interface while the W/$WO_x$ contact is ohmic. This is in agreement with the reported values of work functions and electron affinities of the materials involved (5.4 eV for Au,[33] 4.8 eV for $WO_3$,[34] 4.3–4.6 eV for W[33]).

Impedance spectra recorded for the as-anodized and air-annealed devices may further confirm the presence of a Schottky junction. **Figure 5** shows a typical impedance behavior

  

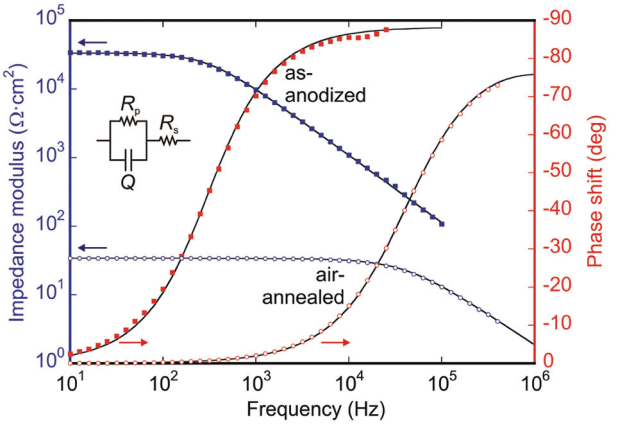


**Figure 5.** The Bode-plot representation of impedance spectroscopy measurements of the MSM devices incorporating the as-anodized and air-annealed $WO_x$ nanorods recorded at RT at 0 V DC bias. The black curves are the fitted spectra; the arrows indicate the corresponding *y*-axis.

of the as-anodized and air-annealed films in Bode-plot representation. The data are fitted with a simple $R_s(R_p$–CPE) circuit, where a constant phase element (CPE) is used to account for frequency dispersion, and the effective device capacitance ($C_{eff}$) is calculated, being 0.033(2) and 0.11(2) μF cm$^{-2}$ respectively. These values correspond to the thickness of a Schottky depletion layer, formed presumably at the tops of the nanorods, of about 54 and 16 nm respectively, providing the relative permittivity ($\varepsilon_r$) of $WO_3$ is 20, assuming that the surface area of the nanorods is about 10% of the apparent device surface area,[26] and meaning that the depletion layer extends only into a small portion of the whole length of the rods, which is about 600 nm over the alumina/tungsten interface. The fitted values of the parallel resistance $R_p$ belonging to the depletion layer correspond to those obtained from the $I(V)$ characteristics (Figure 4b) at 0 V. The serial resistance $R_s$ associated with the materials of the rods and electrodes is incomparably low and could be neglected.

A comparison of the RT data relevant to Schottky junction at the Au/$WO_x$ interface of the MSM microcells tested here (Figure 1e) with those obtained for a depletion layer formed at a solution/$WO_x$ interface of similarly prepared anodic films (as in Figure 1d) reported in a previous work[26] is shown in Table S1 (Supporting Information). Comparable capacitance values and the trend of resistance drop in the order as-anodized → air-annealed → vacuum-annealed nanorods are obvious for both film assemblies. The sequence may be due to the differences in the crystal structure of the rod material:[26] the as-anodized nanorods are amorphous whereas the air- and vacuum-annealed nanorods comprise, respectively, $WO_3$ and $WO_{2.9}$ crystal phases at their tops (Figure 2). The 2–3 orders of magnitude higher resistance of the as-anodized nanorods relative to the air-annealed rods cannot be explained only by the thicker depletion layer, but rather by its amorphous nature because amorphous oxides usually exhibit lower electron conductivity relative to their crystalline counterparts.[35] Additionally, the concentration of oxygen vacancies, serving as the electron donors, may be lower at the tops of the as-anodized nanorods or the Schottky barrier could be higher, as indicated by the thicker depletion layer at the Au/$WO_x$ interface. The resistance of the vacuum-annealed nanorods comprising $WO_{2.9}$ phase is 4 orders of magnitude lower than that of the air-annealed nanorods having $WO_3$ at their tops. This is in agreement with the nature of $WO_{2.9}$ phase, being an n-type degenerate semiconductor,[36] and is supported by the reported values of conductivities of differently doped phases of $WO_3$ (10–10$^{-4}$ S cm$^{-1}$)[1] and $WO_{2.9}$ (10$^3$ S cm$^{-1}$).[36]

To gain a deeper insight into the Schottky-junction nature of the respective interfaces of the MSM microcells incorporating the as-anodized and air-annealed nanorods, temperature-dependent $I(V)$ curves were recorded, as shown in **Figure 6** together with corresponding $R_{dif}(V)$ plots. The narrower voltage range of 0 ± 1.0 V was chosen to minimize the effect of resistance decrease due to the higher voltage applied, as observed during the RT measurements. Three main effects of elevated temperature on the electrical behavior of both types of the MSM devices are worth mentioning. (1) The resistance of the nanoarrays decreases systematically by several orders of magnitude with raising the temperature, as shown in Figure 6h by plotting the temperature dependence of $R_{dif}$ at 0 V, the resistance drop being more pronounced for the as-anodized samples. The decreasing $R_{dif}$ value, regardless of the bias polarity, is associated with semiconducting properties of the $WO_x$ nanorod arrays. (2) The $I(V)$ curves exhibit increasingly asymmetric temperature-dependent electron transport properties, being inverse with respect to the higher-voltage RT behavior (Figure 4), i.e., with a steeper current rise when the upper electrode is negatively biased. Over about 100 °C, the diode-like $I(V)$ behavior becomes significantly enhanced in the as-anodized nanorods, with a current difference of 2 orders of magnitude between the positive and negative bias polarities, compared with only twice as different values of current that flows through the air-annealed nanorods. (3) The onset forward potential is going to zero with increased temperature, as shown in Figure 6g for the as-anodized sample. For the air-annealed film, the exact position of the onset potential cannot be defined and does not change much with operating temperature, taking the range of –0.2 to –0.1 V.

The asymmetric $I(V)$ behavior of the as-anodized films at elevated temperature, contrasting with the inverse behavior at RT, being dramatically enhanced beyond 100 °C and showing a substantially earlier and sharper current rise, implies that, when operating temperature is raised, a Schottky barrier is created at the opposite, i.e., W/$WO_x$ interface, which forms between the substrate metal (W) and the bottom parts of the oxide nanorods. Considering the relatively low work function of W (4.3–4.6 eV)[33] and the observed high thermal sensitivity of the W/$WO_x$ interface, we assume that the barrier is relatively weak and unstable. The reverse current begins to gradually increase rather soon with increasing the temperature owing to temperature-stimulated thermionic emission, while the rectifying effect of the W/$WO_x$ junction strengthens (Figure 6a). This also suggests that the upper (Au/$WO_x$) interface, which forms between the gold electrode and the tops of the rods, gives an ohmic-like contact or, alternatively, a Schottky-like junction that is, however, too low to compete with the barrier at the W/$WO_x$ interface at elevated temperature.

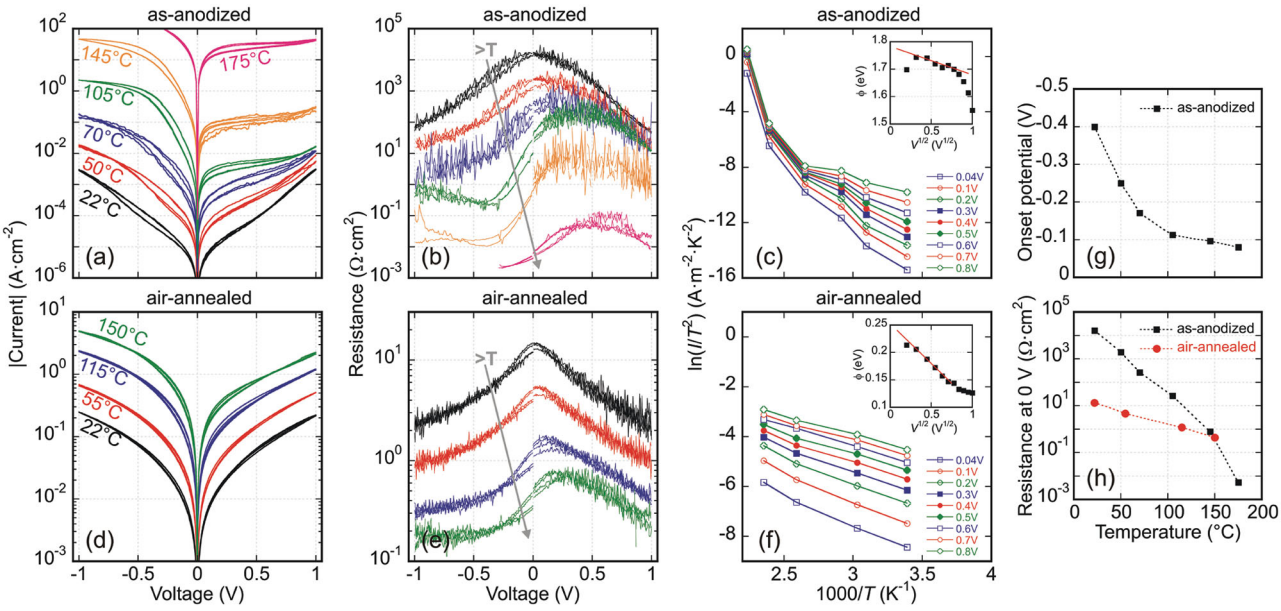


**Figure 6.** Experimental a,d) $I(V)$ and b,e) $R_{dif}(V)$ curves recorded at elevated temperature for the MSM microdevices incorporating the a,b) as-anodized and d,e) air-annealed PAA-inbuilt $WO_x$ nanorods. c,f) Richardson plots ($\ln I/T^2$ vs $1000/T$) calculated from the currents at the positive bias on the top Au electrode (shown in panels (a) and (d)) for the as-anodized and air-annealed devices, respectively, to reveal the Schottky barrier height (shown as inserts in panels (c) and (f)). g) The onset potential vs operating temperature for the as-anodized $WO_x$ nanorods (as estimated from log–log representations of the $I(V)$ curves at the negatively biased top electrode, shown in the Supporting Information). h) Resistance vs operating temperature at 0 V bias voltage for the as-anodized and air-annealed $WO_x$ nanorods.

An intermediate situation arises with the air-annealed nanorods, where the Schottky barrier is lower than that in the as-anodized samples, manifested by the lower resistance and a smaller extent of rectification. The asymmetric $I(V)$ behavior at elevated temperature is also determined by the W/$WO_x$ Schottky junction, as assumed from the sharper current rise when the negative bias is applied to the top (Au) electrode (Figure 6d).

In order to confirm the dominating contribution of the W/$WO_x$ Schottky interface for both the as-anodized and air-annealed samples at elevated temperature and possibly estimate the corresponding Schottky-barrier heights, we plotted the $I(V)$ temperature dependencies as log$I$ vs log$V$ and log$I$ vs $V^{1/2}$ for the different polarizations of the top (Au) electrodes (see Figure S1 in the Supporting Information). A qualitative comparison of features present in $I(V)$ characteristics for an ideal Schottky W/$WO_x$ interface with those revealed in the experimental temperature-dependent $I(V)$ curves for the two film types is given in Table S2 in the Supporting Information. As the log$I$ vs $V^{1/2}$ plots at positive polarization of the top (Au) electrode, which is the reverse direction, show linear dependencies above ≈0.15 V (Figure S1b,f, Supporting Information), we consider the Schottky emission as the main conduction mechanism in the given voltage range, expressed by the following equation[32,37]

$$I_R = A^* \times T^2 \times \exp\frac{-q\left(\phi_B - \sqrt{\frac{q}{4\pi\varepsilon d}} \times \sqrt{V_R}\right)}{kT} \quad (1)$$

where $I_R$ is the reverse current density, $A^*$ is the effective Richardson constant, $\phi_B$ is the Schottky barrier height, $\varepsilon$ is the permittivity of $WO_3$, and $d$ is the depletion layer thickness. From this relation, a linear dependence in the log$I_R$ vs $V_R^{1/2}$ representation is expected, which is indeed obtained for the as-anodized and air-annealed films. We may rewrite Equation (1) as follows

$$\ln\frac{I_R}{T^2} = \ln A^* - \frac{1}{T} \times \frac{q}{k}\left(\phi_B - \sqrt{\frac{q}{4\pi\varepsilon d}} \times \sqrt{V_R}\right) \quad (2)$$

and create so-called Richardson plots, $\ln I/T^2$ vs $1/T$, for selected voltages, which are shown in Figure 6c,f for the as-anodized and air-annealed films and ideally are linear dependencies. By multiplying their slope by $k/q$ and plotting against $V^{1/2}$ (see insets of Figure 6c,f), one can obtain the Schottky-barrier height, $\phi_B$, as the $y$-axis intercept and can also get the thickness of the depletion layer, $d$, from the slope of the plots in the inset graphs: slope $= -(q/4\pi\varepsilon d)^{1/2}$. Thus, the air-annealed sample gives a $\phi_B$-value of 0.25 eV and a $d$-value of 3.6 nm. However, the as-annealed films show rather two slopes in the Richardson plots, the higher-temperature one being considered more reliable, leading to a $\phi_B$-value of 1.78 eV and a $d$-value of 5.6 nm. Considerations of this calculation at the reversed bias polarity yielding relevant $\phi_B$-values, as well as additional calculations at the forward bias, and a discussion of possible contribution of Frenkel–Poole emission transport[32,38] are given in the Supporting Information.

In spite of some uncertainties in fitting the data, introduced by the thermal instability of the Au/$WO_x$ interface,

  

the following conclusions can be drawn. (1) With raising the temperature, in both the as-anodized and air-annealed films, the bottom ($W/WO_x$) interface behaves like a Schottky junction, contrasting with the RT situation when a Schottky barrier forms at the upper ($Au/WO_x$) interface. (2) The $\phi_B$-value calculated for the as-anodized films (0.5–2.2 eV) is obviously higher than that obtained for the air-annealed films (0.2–0.3 eV). The *d*-value for the bottom $W/WO_x$ depletion layer is about 5 nm for both film types.

A well-defined Schottky junction may not form at the $Au/WO_x$ interface at elevated temperature because the work function of a mixture of amorphous $WO_3$, $WO_2$, and $Al_2O_3$ composing the upper parts of the as-anodized rods[26] may be comparable to, or exceeding, that of Au (5.4 eV),[33] so that the formation of an ohmic contact is quite feasible. Moreover, the $Au/WO_x$ interface is likely to give an impeded contact and may have an uneven depth profile owing to the point electrodeposition of gold and possible partial mixing of the materials at the interface. At the $W/WO_x$ interface, due to the absence of extraneous bodies, an intimate (true) contact is formed by the strongest short-range forces. Further, due to a specific chemical composition of the bottom parts of the rods, which are mainly substoichiometric $WO_3$, the work function of the material may also differ from the reported values. This may result in the formation of a more pronounced Schottky-like junction at the $W/WO_x$ interface at elevated temperature. A similar phenomenon of forming a Schottky contact at a $W/WO_x$ interface, even at RT, has been reported by Kim et al.[39] in course of studying electrical properties of thin $WO_3$ films. Additionally, surface states present at the interfaces, which might be also influenced by the residues of adventitious carbon (at the $Au/WO_x$ interface), may also contribute to the formation of a potential barrier, which may impact electron transport in the MSM microcells.[31,32,40]

The substantially lower $W/WO_x$ Schottky barrier in the air-annealed films relative to the as-anodized films may result from chemical and crystallographic changes in the material composing the bottom parts of the rods. The diffusion of oxygen ions into the metal during the heating makes the bottoms of the rods more oxygen-depleted relative to the as-anodized films, thus leading to the formation of $WO_{2.9}$ phase and a more ohmic-like contact at the $W/WO_x$ interface. This is obvious from both the low Schottky barrier and the weak rectification behavior at elevated temperature of the air-annealed films compared to the as-anodized films. Moreover, the depletion layer that forms at the bottom interface of both the as-anodized and air-annealed films at elevated temperature, about 5 nm thick, is much thinner than that formed at the tops of the rods at RT, being 54 and 16 nm, respectively. We assume that this is caused by a relatively higher concentration of oxygen vacancies at the bases of the rods with respect to their tops,[26] rather than by a higher Schottky barrier formed at the upper ($Au/WO_x$) interface at RT compared with that of the bottom ($W/WO_x$) interface at elevated temperature. This is especially true for the as-anodized films, in which a relatively high $W/WO_x$ Schottky barrier forms.[40,41]

Additionally to the contact phenomena at the top and bottom interfaces, the conductance along the nanorods contributes to the overall electron transport in the films. Beside the inner part of the rods having inherent oxygen vacancy concentration, the electronically unsharp $Al_2O_3/WO_x$ interfaces having a mixed composition with a gradient in the alumina content[24,26] may be considered as the shells of the rods influencing the conductivity, for example, through their dielectric nature or by changing the concentration of electron traps at the surface of the rods.[42] In the case of the PAA-inbuilt as-anodized and air-annealed nanorod arrays, the effect of the Schottky interfaces on the overall electron conductance is most essential, as becomes evident from the RT capacitance measurements and the asymmetric $I(V)$ characteristics. The situation, however, may change if the alumina surrounding the rods is removed via chemical dissolution. The "naked" rods may gain higher or lower electron conductance and may demonstrate a different type of $I(V)$ characteristics, with a higher impact of the conductance along the rods on the overall electron transport in the films. This issue may be addressed in a future work.

From a practical view-point, the nanorod arrays developed here may sustain a current density as high as 100 A $cm^{-2}$ without causing an electric breakdown or blistering damage of the materials composing the films. The achievement is explained by the parallel conduction model, which posits that a Schottky barrier is essentially a collection of a very large number of nanoscale diodes in parallel ($\approx 7 \times 10^8$ $cm^{-2}$), with the net $I(V)$ characteristic of the junction collecting the currents of about 0.1 μA carried by each metal-oxide nanorod.

### 2.3. Memristive Electrical Switching

The as-anodized $WO_x$ nanorods assembled in the $Au/WO_x/W$ microcells described in the previous section reveal resistive switching properties at RT with the following major characteristics. (1) The devices are switched from the virgin state into the low-resistance state (LRS) during $I(V)$ cycling to increased voltage applied under both the positive and negative polarization of the top Au electrode (**Figure 7**a). The value of forming voltage, represented by an abrupt current jump to the current compliance limit, is slightly higher in the case of the positive bias, ranging from 2.0 to 2.5 V. Additionally, the asymmetric character of the $I(V)$ curves due to the presence of an $Au/WO_x$ Schottky barrier at RT, as described above, becomes better pronounced with extending the voltage range. (2) After the forming step, bipolar resistive switching is observed with a reset process taking place at the positive polarity at the top Au electrode, manifested by a gradual decrease in measured current, leading to transformation of the device into a high-resistance state (HRS), followed by a consecutive set process at the negative bias polarity typically represented by an abrupt current jump (Figure 7b). The switching polarity is independent of the voltage bias polarity of the forming step. (3) The value of film resistance in the HRS is dependent on the maximum voltage applied during the reset process (Figure 7c), whereas consecutive $I(V)$ sweeps to the same maximum voltage do not lead to any further resistance rise. However, the HRS resistance cannot be tuned by the maximum voltage in a defined manner, and it varies by up to two orders of magnitude within a group of 15 tested devices. (4) A higher value of set voltage is required to switch a higher-resistance HRS into LRS, as depicted in Figure 7d.

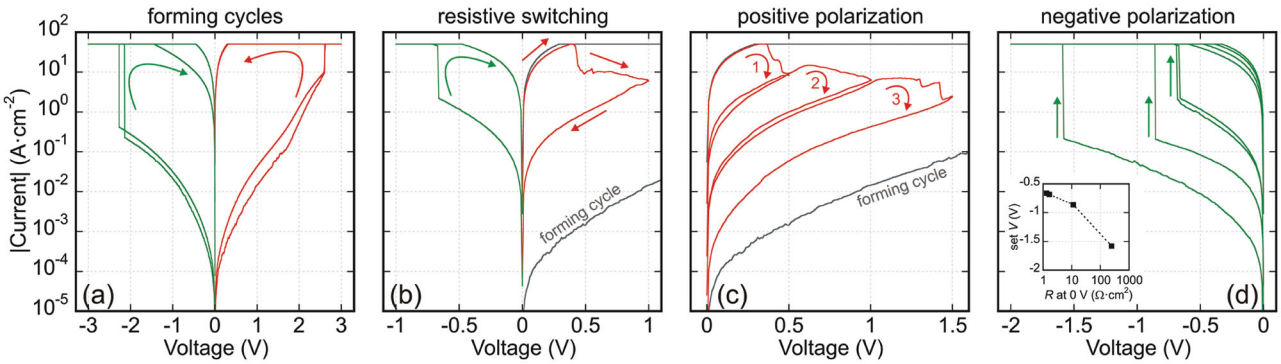


**Figure 7.** Experimental *I*(*V*) curves showing memristive electrical switching in the MSM microdevices incorporating the as-anodized PAA-inbuilt $WO_x$ nanorods (RT, top (Au) electrodes are biased). a) Bias-polarity independent forming cycles for four individual microdevices. b) Bipolar resistive switching, which is independent of the polarity of the forming step, with a gradual reset developing at the positive polarization, followed by a set process at the negative bias. c) Three consecutive reset processes for tuning the HRS resistance by changing the value of the positive voltage bias. d) Set processes for several devices having different resistances in their HRS. The set voltage is dependent upon the HRS resistance value, as depicted in the inset graph.

This kind of resistive switching behavior can be explained as being due to the electric-field-driven movement of oxygen vacancies and thus induced changes in the Schottky junction that forms at the Au/$WO_x$ interface and dominates the transport properties at RT,[29,38,39,41,43] as depicted in detail in **Figure 8**. The nature of the forming process appears to be bias-polarity dependent. In case of the positive bias polarity during the forming step (Figure 8a), the Schottky junction at the Au/$WO_x$ interface is in forward direction, resulting in almost uniform potential distribution along the rods. Oxygen vacancies are repelled from the top electrode and start to accumulate[29] near the oxygen-deficient $WO_x$ phase present at the bottoms of the nanorods.[26] A conducting filament is created in this way reaching the upper Au/$WO_x$ interface, connecting electrically the two electrodes. The filament may be composed of extended defects in the amorphous nanorods, like vacancy chains or shear planes;[29] eventually a conducting Magnéli phase may crystallize[44] due to the Joule heat locally generated via vacancy and electron drift.[43] Another situation arises at the negative voltage bias polarity of the forming step (Figure 8b). In such case, the Au/$WO_x$ Schottky junction is in reverse direction, and most of the applied voltage drops across the depletion layer at the Au/$WO_x$ interface, being about 50 nm thick as estimated from the impedance measurements, leading to oxygen-vacancy drift mainly within the depletion layer. A conducting filament is likely to form in the same way as under the positive forming bias, altering the barrier and thus modifying the electron transport properties of the oxide nanorods. In most of the tested devices, the resistances of the two LRSs were very similar, ranging from about 0.005 to 0.02 Ω cm$^2$, although one may expect a bigger difference. As can be seen, the active interface for the resistive switching after the two forming tactics is still the Au/$WO_x$ junction, and this explains the identical direction of the bipolar resistive switching being independent of the voltage bias polarity of the forming step.

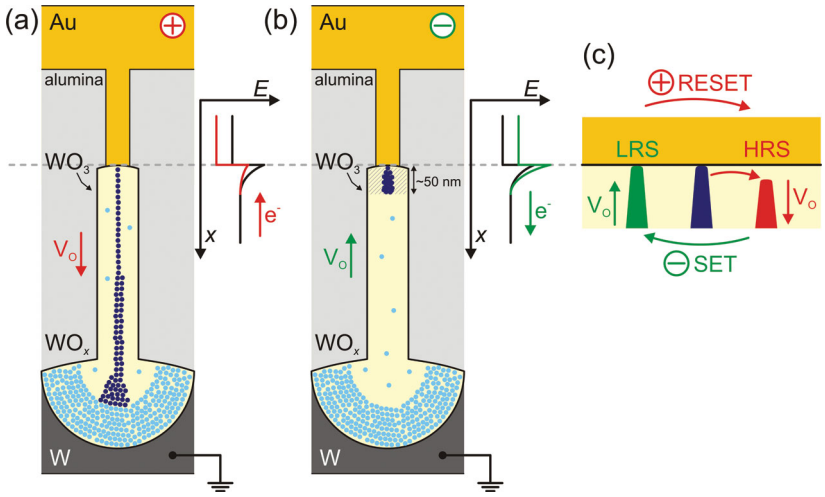


**Figure 8.** Schematic illustrations of the forming processes during the a) positive and b) negative polarization of the top Au electrode of the MSM microdevices employing the as-anodized PAA-inbuilt nanorods. A conducting filament is created either a) within the whole length of a nanorod, growing from the bottom at the positive bias polarity applied at the top electrode or b) only in the upper part of a nanorod within the depletion layer of the original Au/$WO_x$ Schottky junction. The light blue circles represent oxygen vacancies in the films in the virgin state, denoting the oxygen-depleted area at the bottoms of the nanorods, whereas the deep-blue circles show oxygen vacancies created during the forming processes. The corresponding motion of electrons and oxygen vacancies due to the drift in electric field is marked by arrows. The band diagrams at the right show the voltage-related changes of the Schottky barrier at the Au/$WO_x$ interface at a zero bias (black curves) and at the commencement of the voltage bias rise (colored curves). c) Bipolar resistive switching takes place at the Au/$WO_x$ interface, regardless of the extent of filament growth.

The subsequent transition from LRS to HRS, happening by a reset process at the positive bias polarity reveals characteristics typical for a gradual reset. Recently, the origin and kinetics of such a reset have been reviewed and thoroughly investigated with $TaO_x$-based structures.[43] The conclusion was that the gradual reset is related to the temperature-accelerated oxygen-vacancy drift and diffusion, combined with a moderate sensitivity of electron transport

  

to the induced changes in the contact barrier. Based on the above consideration, the reset process shown in Figure 7b,c can be described qualitatively as follows. At the positive bias polarity, the oxygen vacancies within the filament are driven away from the Au/$WO_x$ interface by the electric field determined by the voltage applied whereas their motion is substantially accelerated by Joule heat generated within the filament,[43] thus regenerating the Schottky junction present at that interface in the virgin state. At the same time, the concentration gradient of built-in oxygen vacancies near the Au/$WO_x$ interface induces a backward diffusion of vacancies, i.e., toward the Au/$WO_x$ interface. In this way, an equilibrium of oxygen-vacancy distribution is promptly achieved at a given voltage, in the order of microseconds,[43] which is much faster as compared with the voltage sweep rate, of about 80 mV $s^{-1}$, and the holding time for each voltage value of 100 ms. This explains why the resistance of the HRS is determined by the maximum voltage applied and does not change under consecutive $I(V)$ sweeps to the same voltage. The electronic barrier related to the equilibrium oxygen-vacancy distribution at a given voltage thus controls the electron transport in the HRS. A space–charge layer is therefore formed at the Au/$WO_x$ interface, the thickness of which increases with amplitude of the reset voltage, as manifested by the higher resistance of HRS formed at a higher voltage (Figure 7c), and may be of few nanometers.[43,45] A consecutive set process under the negative bias polarity leads to field-driven motion of oxygen vacancies back into the space–charge layer, recreating the conducting filament and switching the device into the LRS. This may be an explanation for the dependence of set voltage upon the HRS resistance plotted in Figure 7d.[46] The reset and set processes and the qualitative changes of the conducting filament are depicted in Figure 8c.

It should be noted that the HRS resistance achieved at certain maximum voltages varies by up to two orders of magnitude between several tested MSM microcells incorporating the as-anodized films. This may be happening if a filament, as shown in Figure 8a,b, is formed within a small portion of the total $1 \times 10^5$ oxide nanorods in a device, because for example of the instability of the Au/$WO_x$ interfaces having impeded contacts as mentioned above. Alternatively, the phenomenon might be due to a spatial confinement of the filament formation,[39] as the diameter of the nanorods and of a reported filament are of the same order, i.e., about 100 and 40 nm,[44] respectively. More experiments are required to explore diverse effects occurring in these highly aligned metal/oxide interfaces through, for instance, altering the potential profile in the depletion layer, modifying the electronic properties of the interfaces by changing the doping level, and relating the conduction mechanisms and resistive switching characteristics to the technological, electrical, and electrolytic conditions for growing these nanostructured metal-oxide nanofilms.

## 3. Conclusion

In this work, we have synthesized arrays of $WO_x$ nanorods highly aligned in the PAA matrix on a thin layer of tungsten on a silicon wafer, and incorporated them into solid-state MSM microdevices by using the original point electrodeposition of gold in and over the PAA nanopores through a photoresist mask. Electron transport effects were studied within the nanorods and across the nanoscale Au/$WO_x$ and W/$WO_x$ interfaces in the as-anodized (amorphous $WO_x$) and annealed (comprising nanocrystalline $WO_3$ and $WO_{2.9}$ phases) samples. These experimental results establish that electrical conduction in the MSM microdevices is controlled by the nanoscale interfaces. At room temperature, in the amorphous $WO_x$ and the air-annealed $WO_3$-phase-containing nanorods, an array of the top Au/$WO_x$ interfaces performs as a Schottky junction while the bottom W/$WO_x$ interfaces behave as an ohmic contact. At elevated temperature, the upper Au/$WO_x$ interfaces turn out to be ohmic-like whereas the bottom W/$WO_x$ interfaces transform into Schottky-like contacts. The effect is substantially enhanced in the as-anodized amorphous $WO_x$ nanorods, having the higher Schottky barrier and exhibiting increasingly pronounced diode-like $I(V)$ characteristics.

Moreover, the MSM devices built up of the amorphous $WO_x$ nanoarrays reveal memristive bipolar electrical switching properties with a gradual reset after a forming step at relatively low bias voltages of 2–2.5 V. The switching processes take place at the upper Au/$WO_x$ interfaces by oxygen-vacancy drift and diffusion in the depletion layer, modifying the Schottky junction and electron transport across the interface. We believe that, by taking into account the differences in each type of resistive switching, tailoring the materials to specific applications will become an active area in the future development of ReRAM using the formation technique developed here. More generally, the Au/$WO_x$/W multijunctions may be used as model structures for exploring the effect of spatial confinement on the formation of the conducting filaments in ReRAMs. Challenges may arise for more specific applications, like sensors, fuel cells, or field-emission devices should it be possible to selectively dissolve away the PAA matrix and leave the bare $WO_x$ nanorods sandwiched between the upper and bottom electrodes. In such case, the rods may gain different electron transport properties worth studying. Photoelectrochemical, optoelectronic, or nanophotonic effects are also expected in the PAA-inbuilt and PAA-free $WO_x$ nanoarrays, which may be the subjects of future works.

## 4. Experimental Section

*Sample Preparation and Characterization*: The initial samples were Al (500 nm)/W (200 nm) bilayers (aluminum-on-tungsten) sputter-deposited onto oxide-coated Si substrates. Aluminum anodizing was carried out in 0.2 M $H_3PO_4$ under a constant current density of 200 mA $cm^{-2}$ and a steady-state potential of 150 V. Re-anodizing was performed at 0.8 mA $cm^{-2}$ up to 450 V. All processes were conducted at RT in a two-electrode PTFE anodizing cell, as described elsewhere.[26] Selected re-anodized samples were annealed in air or in vacuum ($10^{-4}$ Pa) at 550 °C during 5 h. Electrodeposition of gold in the alumina nanopores was performed from a neutral, buffered $KAu(CN)_2$ bath (pH 6.3) at 50 °C[28,47] through a photoresist mask prepared by a standard photolithography (photoresist AZ 5214E and developer AZ 721 (MIF), both from Microchemicals GmbH). The photoresist layer was removed and all samples were heated to 200 °C to improve Au adhesion. A Tescan MIRA II scanning electron microscope was used for SEM observations of the surfaces and cross fractures of films before and

after selective dissolution of the PAA overlayer. XPS analysis was carried out with a Kratos Axis Ultra DLD spectrometer using a monochromatic Al K$\alpha$ source. The X-ray emission energy was 150 W with a 15 kV accelerating voltage, typical operating pressures were $10^{-9}$ Torr, fixed pass energy for the high-resolution spectra was 20 eV. Spectra were analyzed using CasaXPS software, version 2.3.16 PR 1.6. More details are described elsewhere.[26]

*Electrical/Semiconductor Measurements*: The as-anodized, air-annealed, and vacuum-annealed $WO_x$ nanoarrays assembled in MSM microcells were electrically characterized at room and elevated temperatures by measuring *I*(*V*) characteristics between the upper (Au) and bottom (W) electrodes. A probe station CASCADE M150 with magnetic micromanipulators, connected to a Keithley 4200 semiconductor analyzer, providing a scan rate of ≈80 mV $s^{-1}$, were used in all electrical measurements. To avoid an electric breakdown in the films, the current was limited to 10 mA with the current compliance of the control system. A homemade hotplate with an integrated K-type thermocouple enabled a temperature range of 20–200 °C. The bottom electrode was grounded in all measurements. The apparent surface area of the devices was used to recalculate measured currents into current densities. Impedance spectroscopy measurements were performed for the as-anodized and air-annealed samples at RT in a shielded dark box. A PGSTAT204 FRA32M Metrohm Autolab potentiostat/galvanostat was used as the impedance analyzer. The measured spectra were fitted using a simple *R*(*R*–CPE) circuit by a computer simulation program Autolab NOVA 1.10. The measurements were performed at 0 V DC bias with 10 mV AC perturbation amplitude, generally in a frequency range from 1 MHz (in some cases from 100 kHz) to 10 Hz.

## Supporting Information

Supporting Information is available from the Wiley Online Library or from the author.

## Acknowledgements

Research leading to these results was supported in part by the Czech Science Foundation (GA ČR) under the grant no.14-29531S and by the Ministry of Education, Youth and Sports of the Czech Republic under the project CEITEC 2020 (LQ1601). The authors would like to thank Rajneesh Mohan and Jakub Kolar for fruitful discussions.

Received: June 3, 2016
Revised: July 28, 2016
Published online: August 29, 2016

[1] H. Zheng, J. Z. Ou, M. S. Strano, R. B. Kaner, A. Mitchell, K. Kalantar-zadeh, *Adv. Funct. Mater.* **2011**, *21*, 2175.
[2] V. Khatko, A. Mozalev, G. Gorokh, D. Solovei, F. Guirado, E. Llobet, X. Correig, *J. Electrochem. Soc.* **2008**, *155*, K116.
[3] C. S. Blackman, X. Correig, V. Katko, A. Mozalev, I. P. Parkin, R. Alcubilla, T. Trifonov, *Mater. Lett.* **2008**, *62*, 4582.
[4] A. Mozalev, R. Calavia, R. M. Vázquez, I. Gràcia, C. Cané, X. Correig, X. Vilanova, F. Gispert-Guirado, J. Hubálek, E. Llobet, *Int. J. Hydrogen Energy* **2013**, *38*, 8011.
[5] S. Vallejos, T. Stoycheva, F. E. Annanouch, E. Llobet, P. Umek, E. Figueras, C. Cane, I. Gracia, C. Blackman, *RSC Adv.* **2014**, *4*, 1489.
[6] X. Shi, I. Y. Choi, K. Zhang, J. Kwon, D. Y. Kim, J. K. Lee, S. H. Oh, J. K. Kim, J. H. Park, *Nat. Commun.* **2014**, *5*, 4775.
[7] T. Stoycheva, F. E. Annanouch, I. Gràcia, E. Llobet, C. Blackman, X. Correig, S. Vallejos, *Sens. Actuators B* **2014**, *198*, 210.
[8] J. Zhang, J.-P. Tu, X.-H. Xia, X.-L. Wang, C.-D. Gu, *J. Mater. Chem.* **2011**, *21*, 5492.
[9] D. Ma, G. Shi, H. Wang, Q. Zhang, Y. Li, *J. Mater. Chem. A* **2013**, *1*, 684.
[10] K. Huang, Q. Pan, F. Yan, S. Ni, D. He, *Phys. E (Amsterdam Neth.)* **2007**, *39*, 219.
[11] A. Wisitsoorat, M. Z. Ahmad, M. H. Yaacob, M. Horpratum, D. Phakaratkul, T. Lomas, A. Tuantranont, W. Wlodarski, *Sens. Actuators B* **2013**, *182*, 795.
[12] P.-C. Chang, Z. Fan, C.-J. Chien, D. Stichtenoth, C. Ronning, J. G. Lu, *Appl. Phys. Lett.* **2006**, *89*, 133113.
[13] F. Hernandez-Ramirez, A. Tarancon, O. Casals, E. Pellicer, J. Rodriguez, A. Romano-Rodriguez, J. R. Morante, S. Barth, S. Mathur, *Phys. Rev. B* **2007**, *76*, 085429.
[14] J. Thangala, S. Vaddiraju, R. Bogale, R. Thurman, T. Powers, B. Deb, M. K. Sunkara, *Small* **2007**, *3*, 890.
[15] J.-R. Ding, K.-S. Kim, *AIChE J.* **2016**, *62*, 421.
[16] Y. Qin, W. Xie, Y. Liu, Z. Ye, *Sens. Actuators B* **2016**, *223*, 487.
[17] J. Zhang, W. Zhang, Z. Yang, Z. Yu, X. Zhang, T. C. Chang, A. Javey, *Sens. Actuators B* **2014**, *202*, 708.
[18] H. Terryn, J. Vereecken, *EMC '91: Non-Ferrous Metallurgy—Present and Future, Institution of Mining and Metallurgy*, Kluwer Academic Publishers, The Netherlands **1991**, p. 473.
[19] G. Knörnschild, A. A. Poznyak, A. G. Karoza, A. Mozalev, *Surf. Coat. Technol.* **2015**, *275*, 17.
[20] W. Lee, S.-J. Park, *Chem. Rev.* **2014**, *114*, 7487.
[21] A. Takenaga, T. Kikuchi, S. Natsui, R. O. Suzuki, *Electrochim. Acta* **2016**, *211*, 515.
[22] A. Jagminas, A. Cesuniene, I. Vrublevsky, V. Jasulaitiene, R. Ragalevicius, *Electrochim. Acta* **2010**, *55*, 3361.
[23] A. Mozalev, M. Sakairi, I. Saeki, H. Takahashi, *Electrochim. Acta* **2003**, *48*, 3155.
[24] A. Mozalev, V. Khatko, C. Bittencourt, A. W. Hassel, G. Gorokh, E. Llobet, X. Correig, *Chem. Mater.* **2008**, *20*, 6482.
[25] S. H. Park, Y. H. Kim, T. G. Lee, H. K. Shon, H. M. Park, J. Y. Song, *Mater. Res. Bull.* **2012**, *47*, 3612.
[26] A. Mozalev, M. Bendova, F. Gispert-Guirado, Z. Pytlicek, E. Llobet, *J. Mater. Chem. A* **2016**, *4*, 8219.
[27] A. Mozalev, R. M. Vázquez, C. Bittencourt, D. Cossement, F. Gispert-Guirado, E. Llobet, H. Habazaki, *J. Mater. Chem. C* **2014**, *2*, 4847.
[28] A. Mozalev, M. Bendova, R. M. Vazquez, Z. Pytlicek, E. Llobet, J. Hubalek, *Sens. Actuators B* **2016**, *229*, 587.
[29] R. Waser, R. Dittmann, G. Staikov, K. Szot, *Adv. Mater.* **2009**, *21*, 2632.
[30] M. M. Lohrengel, T. R. Münninghoff, *Galvanotechnik* **2010**, *101*, 730.
[31] K. C. Kao, *Dielectric Phenomena in Solids*, Elsevier Academic Press, London, UK **2004**.
[32] S. M. Sze, K. K. Ng, *Physics of Semiconductor Devices*, John Wiley & Sons, Inc., Hoboken, NJ **2007**.
[33] D. R. Lide, *CRC Handbook of Chemistry and Physics, 82nd Edition*, CRC Press LLC, Boca Raton, FL **2002**.
[34] M. G. Walter, E. L. Warren, J. R. McKone, S. W. Boettcher, Q. Mi, E. A. Santori, N. S. Lewis, *Chem. Rev.* **2010**, *110*, 6446.
[35] A. Mozalev, M. Sakairi, H. Takahashi, H. Habazaki, J. Hubálek, *Thin Solid Films* **2014**, *550*, 486.
[36] G. Kieslich, I. Veremchuk, I. Antonyshyn, W. G. Zeier, C. S. Birkel, K. Weldert, C. P. Heinrich, E. Visnow, M. Panthöfer, U. Burkhardt, Y. Grin, W. Tremel, *Phys. Chem. Chem. Phys.* **2013**, *15*, 15399.
[37] K. P. Biju, X. Liu, M. Siddik, S. Kim, J. Shin, I. Kim, A. Ignatiev, H. Hwang, *J. Appl. Phys.* **2011**, *110*, 064505.
[38] S. M. Hong, H.-D. Kim, M. J. Yun, J. H. Park, D. S. Jeon, T. G. Kim, *Thin Solid Films* **2015**, *583*, 81.
[39] S. Kim, K. P. Biju, M. Jo, S. Jung, J. Park, J. Lee, W. Lee, J. Shin, S. Park, H. Hwang, *IEEE Electron Device Lett.* **2011**, *32*, 671.

  

[40] D. S. Shang, L. Shi, J. R. Sun, B. G. Shen, F. Zhuge, R. W. Li, Y. G. Zhao, *Appl. Phys. Lett.* **2010**, *96*, 072103.
[41] K. P. Biju, X. Liu, S. Kim, M. Siddik, J. Shin, J. Lee, H. Hwang, *Curr. Appl. Phys.* **2011**, *11*, e62.
[42] W. Kim, T. Tachikawa, D. Monllor-Satoca, H. Kim, T. Majima, W. Choi, *Energy Environ. Sci.* **2013**, *6*, 3732.
[43] A. Marchewka, B. Roesgen, K. Skaja, H. Du, C.-L. Jia, J. Mayer, V. Rana, R. Waser, S. Menzel, *Adv. Electron. Mater.* **2016**, *2*, 1500233.
[44] Z.-H. Tan, R. Yang, K. Terabe, X.-B. Yin, X.-D. Zhang, X. Guo, *Adv. Mater.* **2016**, *28*, 377.
[45] K. M. Kim, B. J. Choi, Y. C. Shin, S. Choi, C. S. Hwang, *Appl. Phys. Lett.* **2007**, *91*, 012907.
[46] Y. Nishi, K. Fleck, U. Böttger, R. Waser, S. Menzel, *IEEE Trans. Electron Devices* **2015**, *62*, 1561.
[47] a) B. Bozzini, A. Fanigliulo, *J. Appl. Electrochem.* **2002**, *32*, 1043; b) P. A. Kohl, in *Modern Electroplating* (Eds: M. Schlesinger, M. Paunovic), John Wiley & Sons, Inc., Hoboken, NJ **2010**, Ch. 4.